HEAT FLUXES AND ROLL CIRCULATIONS OVER THE WESTERN GULF STREAM DURING AN INTENSE COLD-AIR OUTBREAK

SHU-HSIEN CHOU and MICHAEL P. FERGUSON*
Laboratory for Atmospheres, NASA/Goddard Space Flight Center, Greenbelt, MD 20771, U.S.A.

(Received in final form 7 November, 1990)

Abstract. Turbulence and heat fluxes in the marine atmospheric boundary layer (MABL) for the roll vortex regime, observed during the Genesis of Atlantic Lows Experiment (GALE) over the western Gulf Stream, have been studied. The spectral analysis suggests that cloud streets (roll vortices) are vertically organized convection in the MABL having the same roll scale for both the cloud layer and subcloud layer, and that the roll spacing is about three times the MABL depth. The roll circulations contribute significantly to the sensible (temperature) and latent heat (moisture) fluxes with importance increasing upward. Near the MABL top, these fluxes are primarily due to roll vortices which transfer both sensible heat and moisture upward in the lower half of the convective MABL. Near the MABL top, the roll circulations transfer sensible heat downward and moisture upward in the clear thermal-street region, but roll vortices influenced by evaporative cooling can transfer sensible heat upward and moisture downward in the cloud-street region. Near the cloud-top, the upward buoyancy flux due to evaporative cooling is highly related to the roll circulations near the inversion.

For the lower half of the MABL, the normalized temperature flux decreases upward more rapidly than the humidity flux, which is mainly because potential temperature (θ) increases slightly upward while humidity (q) decreases slightly upward above the unstable surface layer. The gradient production (associated with the θ gradient) is a source for the temperature flux in the unstable surface layer but changes to a sink in the mixed layer, while the gradient production (associated with the q gradient) acts as a source for the humidity flux in both the unstable surface and mixed layers. The results suggest that the entrainment at the MABL top might affect the budgets of temperature and humidity fluxes in the lower MABL, but not in the unstable surface layer.

1. Introduction

The maximum net annual heat loss from the North Atlantic to the atmosphere occurs in the area off the North Carolina coast of the United States over the warm Gulf Stream (Budyko, 1963; Bunker and Worthington, 1976). The heat loss is maximized during cold-air outbreaks (Agee and Howley, 1977), due to large sea-air temperature and humidity differences coupled with strong offshore winds. This area, which appears to be a preferred region for rapid cyclogenesis (e.g., Reitan, 1974; Sanders and Gyakum, 1980), was chosen for the Genesis of Atlantic Lows Experiment (GALE) from 15 January to 15 March 1986 (Dirks et al., 1988). The ocean-to-air heat fluxes over the warm water of the Kuroshio Current (off the coast of China) and the Gulf Stream are known to have profound effects on cyclogenesis and storm intensification (Agee and Howley, 1977). These fluxes are

---

* Caelum Research Corporation, Silver Spring, MD 20901, U.S.A.

Boundary-Layer Meteorology **55**: 255–281, 1991.

also related to the prevailing synoptic and mesoscale disturbances (Warsh, 1973; Sheu and Agee, 1977; Kung and Siegel, 1979). One of the objectives of GALE was to investigate the heat transport mechanisms associated with airmass transformation during cold-air outbreaks.

An intense cold-air outbreak, with the sea surface temperature (SST) warmer than the 70-m level air temperature by ≈ 19–24 °C, occurred offshore of the Carolinas in the GALE area on 28 January 1986 (Figure 1). The GOES visible image shows that cloud streets, with axes nearly parallel to the mean Marine Atmospheric Boundary Layer (MABL) wind directions, prevailed over the Gulf Stream. The purpose of this paper is to study the turbulence structure in the MABL for this case and the significance of roll vortices to heat fluxes. Mixed-layer scaling has generally been used to investigate the turbulence, diffusion, and dominant eddies in a convective boundary layer (e.g., Deardorff, 1972, 1985; Willis and Deardorff, 1974; Kaimal *et al.*, 1976; Lenschow *et al.*, 1980, hereafter LWP; Chou *et al.*, 1986). The same scaling is also adopted to analyze the data in this study.

There have been several boundary-layer studies for this cold-air outbreak. Chou and Zimmerman (1989, hereafter CZ), have used a bivariate conditional sampling technique to investigate the generation of buoyancy flux in the lower half of the MABL (subcloud layer), as measured by both the NCAR Electra and King Air aircraft. Grossman and Betts (1990), adjusting the temperature data measured by the NCAR Electra for the effects of diurnal variation at the shore, have studied the Lagrangian budgets of temperature and moisture in the subcloud layer. Bane and Osgood (1990) have discussed the oceanic response to this cold-air outbreak.

2. Data Analysis

Figure 1 shows the GOES visible image, NCAR Electra (E1, E2, E3, and E4) and King Air (K1 and K2) aircraft crosswind stack locations, and the western and eastern Gulf Stream fronts for the GALE 28 January 1986 case. In this study, 3 stacks (K1, E1, and E2) near the western Gulf Stream front have been chosen for analysis. The turbulent quantities were measured by gust-probe systems (Wyngaard *et al.*, 1978, hereafter WPLL; LeMone and Pennell, 1980). The turbulence data were recorded at 50 samples per second. All of the variables were low-pass filtered with digital four-pole low-pass Butterworth filters with a 10-Hz cutoff frequency and then interpolated to a sampling rate of 20 Hz.

The fast-response absolute humidity was estimated from the Lyman-Alpha hygrometer, which was calibrated using linear regressions with the measurements of a slower-response thermoelectric dewpoint hygrometer (Friehe *et al.*, 1986; CZ). According to the method of Friehe *et al.*, the regression slope (important for estimating humidity flux and variance) and intercept may be determined from both low-pass time series using a Lanczos (1956) filter. However, the slope and intercept depend on the cutoff frequency of the filter. Grossman (personal com-

GOES VISIBLE 28 JANUARY 1986 1800 GMT

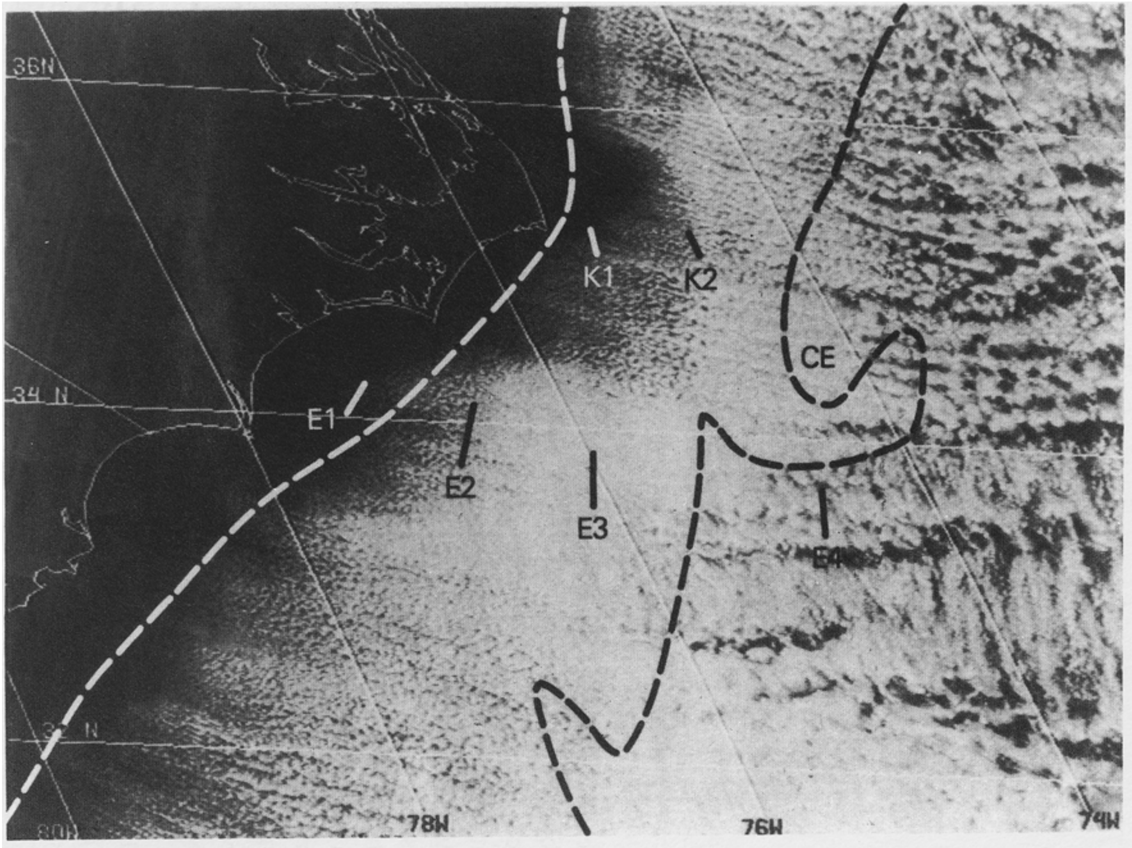

Fig. 1. The GOES visible image, NCAR Electra (E1, E2, E3, and E4) and King Air (K1 and K2) aircraft crosswind stack locations, and the western and eastern Gulf Stream fronts for the GALE 28 January 1986 case. The symbol "CE" indicates cold eddy of ocean current.

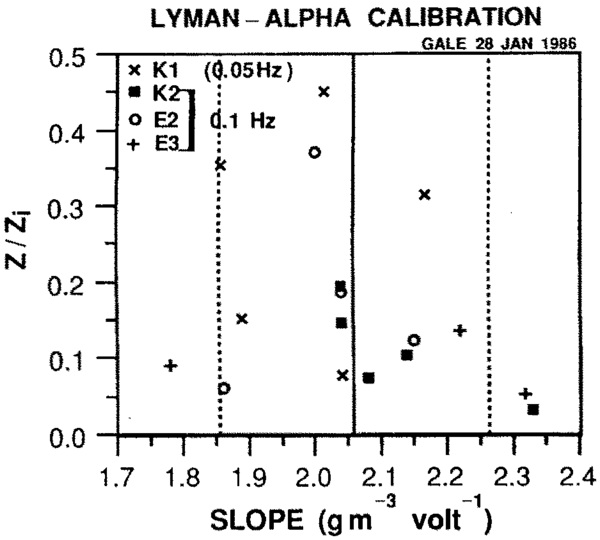

Fig. 2. Vertical distributions of regression slopes of the Lyman-Alpha calibration based on Friehe *et al.* (1986) for subclouds at stacks K1, K2, E2, and E3 (see Figure 1). The filter frequency is 0.05 Hz for K1 and 0.1 Hz for others. The solid line indicates the mean slope (2.057 $\mathrm{gm}^{-3}\,\mathrm{V}^{-1}$), and the dashed lines ±10% deviations from the mean. The height Z is normalized by the inversion base height, Z_i.

munication, 1989) has suggested that the correlation coefficient of linear regression may be used as a guide to determine the best filter frequency.

Except for the poor calibration near inversion bases and at E1 (due to dryness) and at E4 (due to a snow shower), the optimum frequencies for the other horizontal flights in the subcloud layers were found to be near 0.05–0.1 Hz. The subcloud regression slopes at K1 (0.05-Hz filter) and those at K2, E2, and E3 (0.1-Hz filter) are shown in Figure 2. The average slope is 2.057 $\mathrm{gm}^{-3}\,\mathrm{V}^{-1}$ (solid line) and the mean correlation coefficient is 0.98. These slopes, except for three data points of K2 and E3, are within 10% of the average (dashed lines) and are without any systematic variation with height, which is in good agreement with the finding of Grossman and Betts based on E2 and E3 only. Therefore, the regression slope of Grossman and Betts (2.066 $\mathrm{gm}^{-3}\,\mathrm{V}^{-1}$) was used to calibrate the Lyman-Alpha data.

A 1-Hz Lanczos filter was used by CZ to calibrate Lyman-Alpha data because they found that the regression slopes were generally not sensitive to the filter frequency near the 1-Hz cutoff frequency. The values of those slopes (1-Hz filter) are 0.5–1, 1.4–1.8, 1.6–1.8, 1.1–1.6, and 1.6–1.9 $\mathrm{gm}^{-3}\,\mathrm{V}^{-1}$ for the lower half of the MABL at E1, E2, E3, K1, and K2, respectively. They are smaller than the value 2.066 $\mathrm{gm}^{-3}\,\mathrm{V}^{-1}$ used in this study and generally increase with height. As compared to this study, the use of the regression slopes with the 1-Hz filter (CZ) will certainly underestimate fluxes and variances of humidity as well as their vertical lapse rates. The impact of this calibration on the surface latent heat flux is further discussed in Section 3.

The turbulence statistics were computed for 5-min segments (about 30 km for the Electra; 23 km for the King Air). Fluctuations of parameters were obtained by removing the mean and the linear trend calculated over each flight segment. The spectra and cospectra were first estimated from the Fourier transforms of the autocovariance and crosscovariance functions, using a Tukey spectral window with a maximum correlation lag of 10 km (Jenkins and Watts, 1968). Using mixed-layer scaling for the normalized frequency (Kaimal *et al.*, 1976), these spectra and cospectra were further averaged to produce normalized spectra and cospectra containing 20 points per decade.

3. Mean Boundary-Layer Structure

Figure 3 shows the weekly mean SST for the period 24–29 January 1986 and the aircraft stack locations. Except for E1, the aircraft stacks were located near the maximum net annual oceanic heat loss to the atmosphere (Bunker and Worthington, 1976). For the 28 January 1986 case, the SST at E1 was about 14 °C and was colder than the weekly average (17.5°C) due to the cold-air outbreak over the cold shelf water at E1. Figure 3 and aircraft data indicate that the crosswind stacks at E1 and E2 were nearly parallel to the SST isotherms, but the stack at K1 was nearly perpendicular to the SST isotherms.

Table I shows the boundary-layer parameters for these three stacks; those of the other stacks were included in CZ and Grossman and Betts (1990). The parameter Z_i is the height of the inversion base, L the Monin–Obukhov length, u_* the friction velocity; $(\overline{w'\theta_v'})_0$, $\rho c_p(\overline{w'\theta'})_0$, and $L_v(\overline{w'q'})_0$ the surface fluxes of buoyancy, sensible, and latent heat, respectively; and ρ, c_p, and L_v air density, heat capacity at constant pressure, and latent heat of condensation, respectively. The mixed-layer velocity, temperature, and humidity scales are defined as (e.g., LWP; CZ)

$$\begin{aligned} w_* &= [(g/\bar{\theta}_v)(\overline{w'\theta_v'})_0 Z_i]^{1/3}\,, \\ \theta_* &= (\overline{w'\theta'})_0/w_*\,, \\ q_* &= (\overline{w'q'})_0/w_*\,. \end{aligned} \tag{1}$$

The stability parameter-Z_i/L suggests that these three stacks were in the roll vortex regime (LeMone, 1973), consistent with the GOES image (Figure 1). The mean MABL wind was generally westerly (270°–280°) and nearly parallel to the cloud streets. The total surface fluxes of sensible and latent heat ranged from 550 (E1) to 1000 (E2) W m^{-2}. The large difference in flux is mainly due to the change in SST across the Gulf Stream front (SST = 14 °C at E1 and 20 °C at E2) and the downwind increase in wind speed.

Both $\rho c_p(\overline{w'\theta'})_0$, and $L_v(\overline{w'q'})_0$ are in good agreement with those of Grossman and Betts. However, the values of $L_v(\overline{w'q'})_0$ are about 190–250 W m^{-2} larger than those of CZ. This difference results from Lyman-Alpha calibration. As

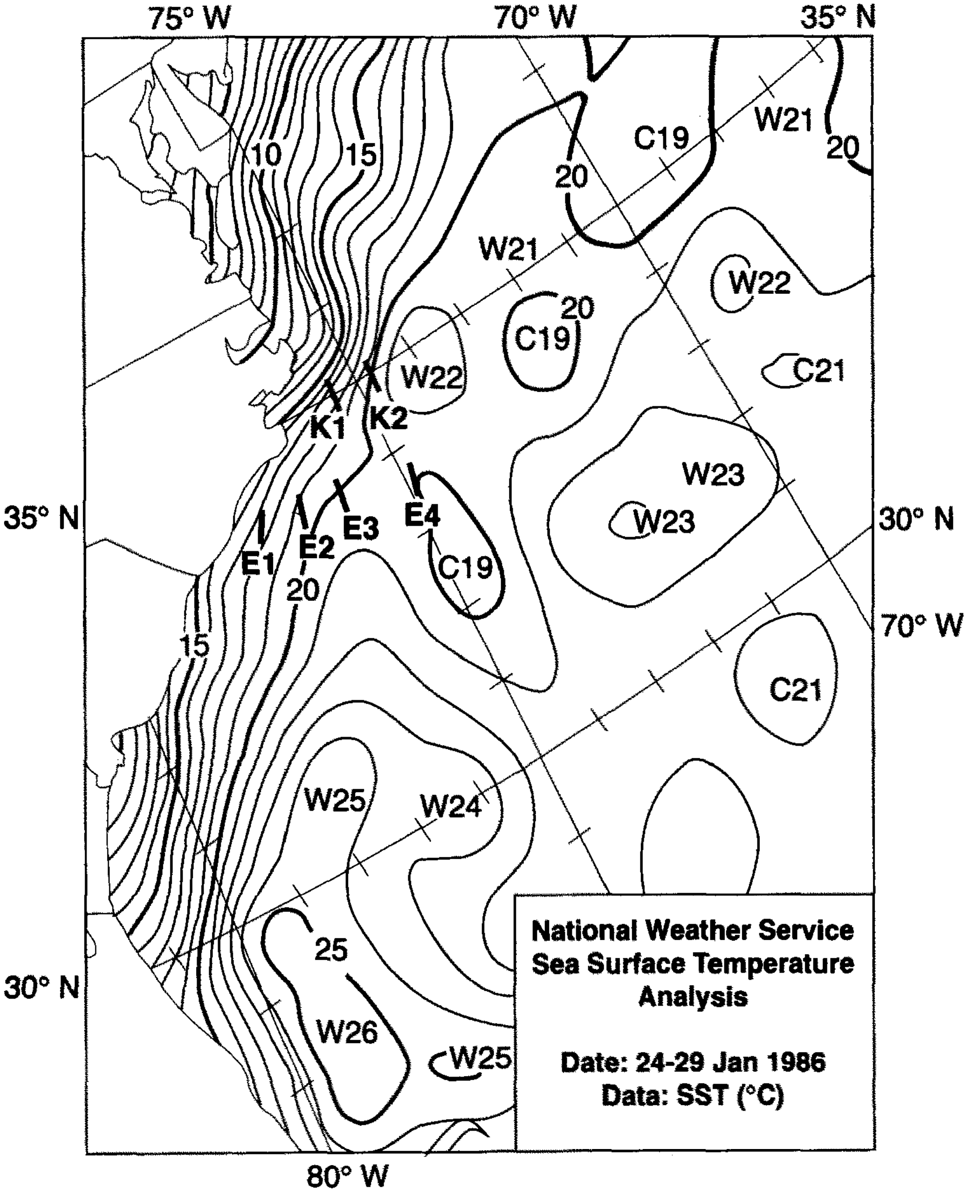

Fig. 3. Weekly mean SST for the period 24–29 January 1986, together with NCAR Electra (E1, E2, E3, and E4) and King Air (K1 and K2) aircraft stack locations for the GALE 28 January 1986 case.

mentioned earlier, the regression slopes of CZ are smaller than that used in this study and generally increase with height. Therefore, their extrapolated values for $L_v(\overline{w'q'})_0$ are smaller. It is noted that $L_v(\overline{w'q'})_0$, computed from the bulk formula of Kondo (1975), is 353 W m^{-2} at Buoy 2 (2000 GMT, near E1) and 676 W m^{-2} at R/V Cape Hatteras (1800 GMT, near E2), which are in good agreement with

TABLE I

Boundary-layer parameters for the GALE 28 January 1986 case

Stack	Z_i (m)	$-Z_i/L$	SST (°C)	u_* (m s^{-1})	w_* (m s^{-1})	θ_* (K)	q_* (g m^{-3})	$(\overline{w'\theta_v'})_0$ (m s^{-1} K)	$\rho C_p(\overline{w'\theta'})_0$ (W m^{-2})	$L_v(\overline{w'q'})_0$ (W m^{-2})
K1	750	11	–	0.67	1.97	0.127	0.085	0.28	328	419
E1	960	9	14	0.66	1.81	0.094	0.072	0.17	222	325
E2	1070	4	20	1.07	2.25	0.129	0.111	0.29	381	626

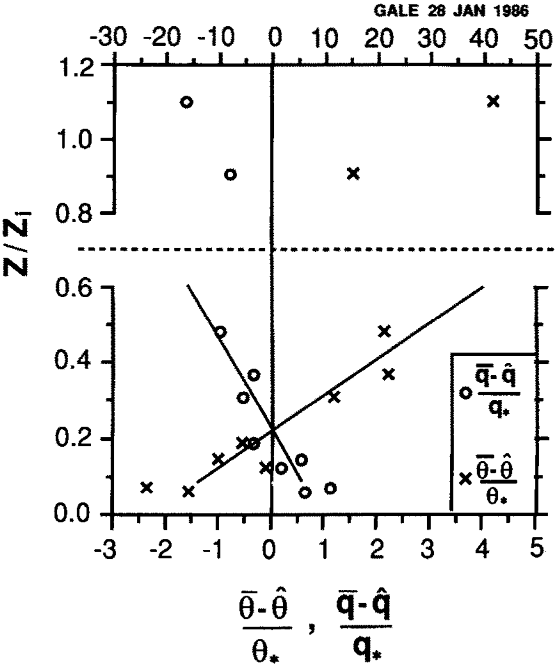

Fig. 4. Vertical profiles of the normalized potential temperature $[(\bar{\theta}-\hat{\theta})/\theta_*]$ and absolute humidity deviations $[(\bar{q}-\hat{q})/q_*]$ from the averages below $0.5Z_i$ $(\hat{\theta}, \hat{q})$ for E1 and E2. Over-bars indicate leg averages. Solid curves are least-squares fits to the data below $0.5Z_i$.

those of this study. These results suggest that the Lyman-Alpha data are better calibrated in this study than in CZ.*

Typical profiles of potential temperature (θ) and absolute humidity (q) may be seen in Figure 4, which shows the composite normalized θ and q deviations from the averages below $0.5Z_i$ $(\hat{\theta}, \hat{q})$ for E1 and E2. The results are in general agreement with previous observational studies (e.g., Pennell and LeMone, 1974; Mahrt, 1976; WPLL; LWP). Near the MABL top (the inversion base), θ increases rapidly upward while q decreases sharply, suggesting strong entrainment effects. Within the MABL above the unstable surface layer (stability can be inferred from Table I), there is a slight increase in θ with height, but a slight decrease in q; the normalized q lapse rate $[(Z_i/q_*)\, \partial\bar{q}/\partial z = -4.12]$ is in good agreement with that of the AMTEX (Air-Mass Transformation Experiment) measurements of LWP and WPLL, while the normalized θ lapse rate $[(Z_i/\theta_*)\, \partial\bar{\theta}/\partial Z = 10.5]$ is 7.5 times larger than that of LWP and WPLL which was derived using the mixed-layer assumption θ_v = constant. The difference in lapse rates between θ and q presumably reflects the fact that the entrainment at the MABL top brings the warmer and drier air down into the MABL (see Figure 8 of CZ). This difference can have

---

* Lyman-Alpha calibration does not affect the results and conclusions of CZ on buoyancy flux because the calibrated Lyman-Alpha data were not used to compute θ_v.

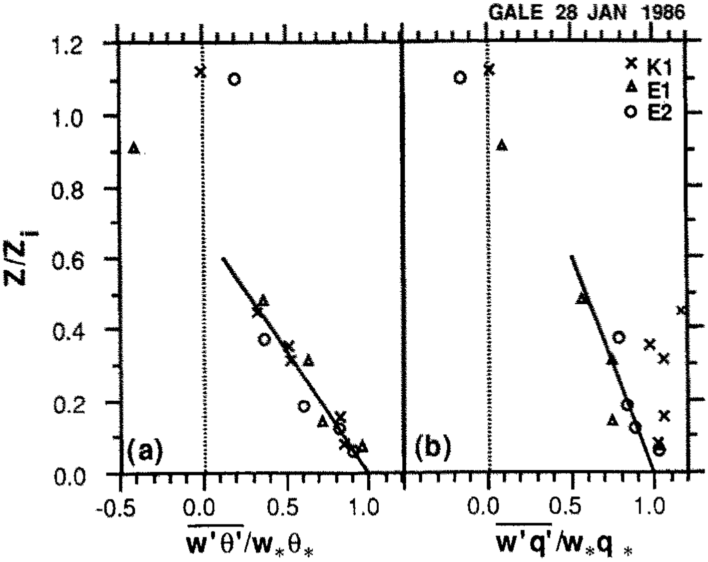

Fig. 5. Vertical profiles of the normalized (a) potential temperature and (b) humidity fluxes. Solid curves are least-squares fits to the data below $0.5Z_i$ (K1 is excluded in $\overline{w'q'}$ fitting).

a significant influence on the vertical profiles of the fluxes and variances of θ and q, as well as their budgets.

4. Fluxes and Variances

Figure 5 shows the vertical profiles of the normalized potential temperature and humidity fluxes. Below $0.5Z_i$, the temperature fluxes are well fitted by the solid curve of Figure 5a,

$$\overline{w'\theta'}/w_*\theta_* = 1 - 1.46(Z/Z_i)\,, \tag{2}$$

which is in good agreement with that derived from the AMTEX data (LWP). On the other hand, the humidity fluxes are not in good agreement with those of AMTEX(WPLL); the flux profiles show large variability in both cases. Nicholls and LeMone (1980) saw considerable variation in $\overline{w'q'}$ depending on cumulus convection. The humidity fluxes at E1 and E2 are well fitted by the solid curve of Figure 5b,

$$\overline{w'q'}/w_*q_* = 1 - 0.83(Z/Z_i)\,, \tag{3}$$

and are quite different from the nearly constant flux profile at K1. It was found that the difference is mainly located in the frequency band containing roll vortices. Near 0.3–$0.5Z_i$ the roll vortices appear to be more organized and more effective in transporting water vapor into the cloud layer at K1 than the other two stacks (see Section 5). This difference is likely to be related to the SST isotherms and

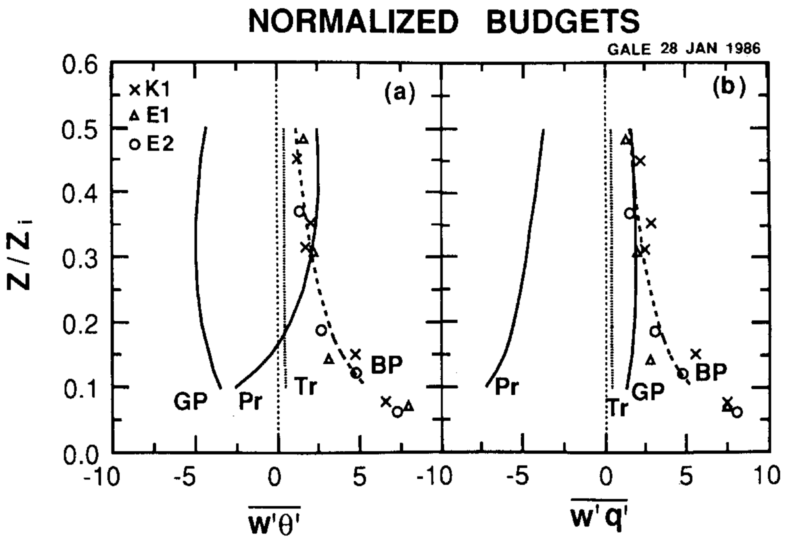

Fig. 6. Normalized budgets of (a) temperature and (b) humidity fluxes; GP (solid lines) indicates gradient production, BP (dashed lines with data points) the buoyancy production, Tr (dotted lines) the turbulent transport, and Pr (solid lines) the pressure transport. The Pr terms are the imbalances of three estimated terms (GP, BP, and Tr) of (4) and (5). (See text for detailed discussion).

their orientations with respect to roll circulations. The axes of cloud streets were nearly parallel to SST isotherms at K1, but were nearly normal to SST isotherms at E1 and E2 (Figures 1 and 3). The updraft branches of the roll circulations at K1 (associated with a stronger SST gradient) are likely to transport buoyant moist air with larger normalized q variance upward from the sea surface. This can enhance the humidity flux through the buoyant production (BP) term for K1, as compared to E1 and E2 (see Figure 6). Indeed, the normalized BP of $\overline{w'q'}$ near the roll frequency band was found to be larger at K1.

Both solid curves in Figure 5 suggest that the subcloud layer may be warmed and moistened by the flux divergences. However, the normalized heating rate is larger than the normalized moistening rate due to the different slopes of the fluxes. The maintenance of both fluxes may be learned from the normalized budgets of temperature and humidity fluxes written as (LWP)

$$\frac{Z_i}{w_*^2\theta_*}\frac{\partial}{\partial t}(\overline{w'\theta'}) = -\frac{\sigma_w^2 Z_i}{w_*^2\theta_*}\frac{\partial\bar{\theta}}{\partial Z} + \frac{\overline{\theta_v'\theta'}}{\theta_{v*}\theta_*} - \frac{Z_i}{w_*^2\theta_*}\frac{\partial}{\partial Z}(\overline{w'^2\theta'}) - \frac{Z_i}{w_*^2\theta_*}\frac{\partial}{\partial Z}(\overline{p'\theta'})\,, \qquad (4)$$

$$\frac{Z_i}{w_*^2 q_*}\frac{\partial}{\partial t}(\overline{w'q'}) = -\frac{\sigma_w^2 Z_i}{w_*^2 q_*}\frac{\partial\bar{q}}{\partial Z} + \frac{\overline{\theta_v' q'}}{\theta_{v*} q_*} - \frac{Z_i}{w_*^2 q_*}\frac{\partial}{\partial Z}(\overline{w'^2 q'})$$

(GP) (BP) (Tr)

$$-\frac{Z_i}{w_*^2 q_*}\frac{\partial}{\partial Z}(\overline{p'q'}) \,, \tag{5}$$

$$\text{(Pr)}$$

where t indicates time, σ_w^2 the variance of vertical velocity (w), $\theta_{v*} = (\overline{w'\theta_v'})_0/w_*$, p the pressure. The first terms on the right of (4) and (5) represent gradient production (GP), which are related to gradients of θ and q; the second terms represent buoyant production (BP); the third terms indicate turbulent transports (Tr), which are related to third moments; and the fourth terms indicate pressure transports (Pr) which are related to the covariances with pressure. Figure 6 shows the normalized budgets of $\overline{w'\theta'}$ and $\overline{w'q'}$ for the layer 0.1–0.5Z_i (above the surface layer). The GP terms were estimated from Figure 4 and the σ_w^2/w_*^2 results of LWP (see Figure 9 for the comparison with this study); the Tr terms were derived from the composite vertical profiles of normalized third moments (see appendix); and the Pr terms were estimated as the imbalances of the other three terms (GP, BP, and Tr) under steady-state conditions. The BP data below 0.5Z_i are well fitted by

$$\overline{\theta_v'\theta'}/\theta_{v*}\theta_* = 1.3(Z/Z_i)^{-2/3}(1 - 0.8Z/Z_i) \,, \tag{6}$$

$$\overline{\theta_v'q'}/\theta_{v*}q_* = 1.2(Z/Z_i)^{-2/3}(1 - 0.3Z/Z_i) \,. \tag{7}$$

Buoyant production (BP) decreases upward slightly more slowly for $\overline{w'q'}$ than for $\overline{w'\theta'}$. However, the difference between (6) and (7) is very small and is within ≈0.3 for 0.1–0.5Z_i. According to (A1) and (A2), turbulent transport (Tr) for $\overline{w'\theta'}$ and $\overline{w'q'}$ are 0.5 and 0.45, respectively. Therefore, the contributions of Tr to both budgets are about the same and much smaller than those of the other budget terms. Figure 6 suggests that the difference in both budgets is mainly due to gradient production (GP) because buoyant production (BP) and turbulent transport (Tr) are about the same for both budgets. Gradient production (GP) is a sink for $\overline{w'\theta'}$ because of positive $\partial\bar{\theta}/\partial Z$, but is a source for $\overline{w'q'}$ due to negative $\partial\bar{q}/\partial Z$ (see Figure 4). The mechanism of GP for $\overline{w'\theta'}$ and $\overline{w'q'}$ may be visualized as follows. For a positive $\partial\bar{\theta}/\partial Z(\partial\bar{q}/\partial Z)$, updrafts tend to carry negative $\theta'(q')$ and downdrafts carry positive $\theta'(q')$. Therefore, the vertical component of turbulent kinetic energy (σ_w^2) destroys $\overline{w'\theta'}(\overline{w'q'})$. The entrainment at Z_i can cause a positive $\partial\bar{\theta}/\partial Z$ and a negative $\partial\bar{q}/\partial Z$ near Z_i and in the mixed layer. In the upper mixed layer, the $\overline{w'\theta'}$ and $\overline{w'q'}$ budgets are strongly influenced by entrainment effects (e.g., Deardorff, 1974; LWP). The large difference in GP between the budgets suggests that the entrainment can also affect both budgets in the lower mixed layer.

For the lower mixed layer (with entrainment effects), buoyant production (BP) and gradient production (GP) are sources for $\overline{w'q'}$ to balance the sink due to pressure transport (Pr), while BP and Pr are sources for $\overline{w'\theta'}$ to balance the sink due to GP. On the other hand, the entrainment effects are generally negligible in the unstable surface layer and both $\partial\bar{\theta}/\partial Z$ and $\partial\bar{q}/\partial Z$ are negative. Therefore, the budgets of $\overline{w'\theta'}$ and $\overline{w'q'}$ are expected to be fairly similar in the unstable surface layer, where GP and BP (buoyant thermals are warm and moist) act as sources for both $\overline{w'\theta'}$ and $\overline{w'q'}$ to balance the sinks due to Pr (e.g., Wyngaard *et al.*, 1971; LWP). The vertical profiles of $\overline{w'\theta'}$ and $\overline{w'q'}$ vary among cases, especially $\overline{w'q'}$ (e.g., Nicholls and LeMone, 1980; Nicholls, 1984; Chou *et al.*, 1986). They can not be determined or predicted from the budget equations. However, the comparison of the budgets should provide some insight about the different behavior of the flux profiles in the same case. As mentioned earlier, the normalized $\overline{w'\theta'}$ decreases upward more sharply than the normalized $\overline{w'q'}$ (Figure 5). Figure 6 suggests that this result is mainly due to the fact that GP is a source for $\overline{w'\theta'}$ in the unstable surface layer but changes to a sink in the mixed layer, while GP acts as a source for $\overline{w'q'}$ in both the unstable surface and mixed layers.

The budget of $\overline{w'q'}$ is in fairly good agreement with that of LWP except that BP decreases (Pr increases) less rapidly upward for this case. The difference in buoyant production (BP) is related to the θ-q correlation (discussed later). On the other hand, the budget of $\overline{w'\theta'}$ is not in good agreement with that of LWP. As compared to the results of LWP, gradient production (GP) is smaller by about 4 (7.5 times more negative) due to larger normalized $\partial\bar{\theta}/\partial Z$, and buoyant production (BP) is smaller by about 1–2. Thus, pressure transport (Pr) acts as a source for $\overline{w'\theta'}$ above $0.2Z_i$, rather than a sink, as estimated in LWP.

The correlation coefficient γ_{xy} can be computed as

$$\gamma_{xy} = \overline{x'y'}/\sigma_x\sigma_y\,, \tag{8}$$

where $\overline{x'y'}$ is the covariance of variables x and y, and σ_x and σ_y the standard deviations of x and y, respectively. The vertical profiles of $\gamma_{q\theta}$, $\gamma_{w\theta}$, γ_{wq} are shown in Figure 7. It can be seen from Figure 7a that $\gamma_{q\theta}$ is ≈ 1 near the surface, in good agreement with previous studies (e.g., Phelps and Pond, 1971; WPLL; CZ). This result is consistent with the finding of CZ that warm, moist rising thermals and cool, dry sinking ambient air prevail over the warm, evaporating sea surface. The correlation $\gamma_{q\theta}$ decreases upward and approaches -1 near Z_i, in good agreement with previous studies (e.g., WPLL; Druilhet *et al.*, 1983; CZ). This result is related to entrainment of warm, dry air from the capping inversion layer and penetration of cool, moist thermals from the lower MABL. As compared to the result of LWP for the lower half of the MABL, $\gamma_{q\theta}$ decreases less rapidly with height; thus buoyant production (BP) for $\overline{w'q'}$ decreases less sharply (Figure 6b). This difference is probably related to the differences in convective regimes and evaporation. The vertical profile of $\gamma_{q\theta}$ (and γ_{wq}) depends on two boundary conditions: the evaporation at the sea surface, and entrainment and penetration at the MABL top (Druilhet *et al.*, 1983). As the roll vortices can concentrate thermals near the roll-scale updraft regions (LeMone, 1976; Grossman, 1982), the effect of strong evaporation will be carried farther upward by the updrafts and $\gamma_{q\theta}$ will be enhanced

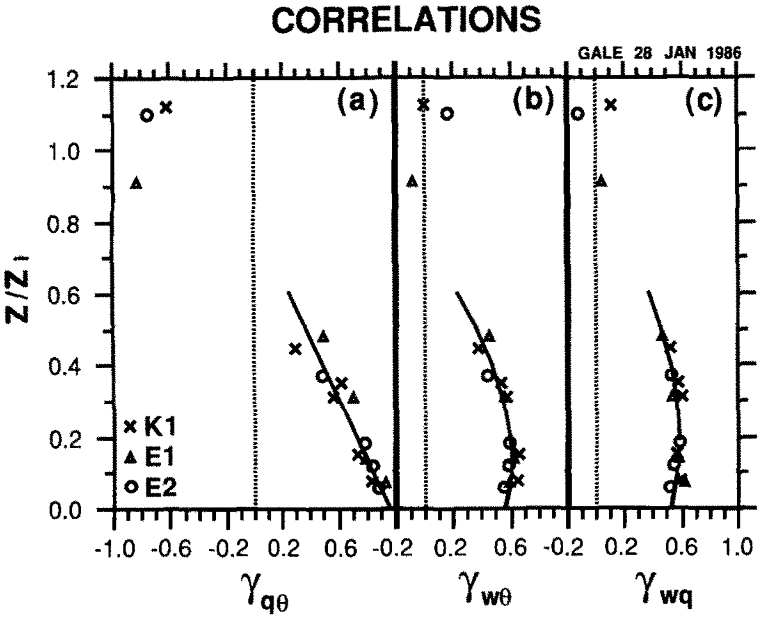

Fig. 7. Vertical profiles of correlation coefficients: (a) humidity and potential temperature, (b) vertical velocity and potential temperature, and (c) vertical velocity and humidity. Solid curves are least-squares fits to the data below $0.5Z_i$.

in the roll vortex regime, as compared to the MCC (mesoscale cellular convection) regime of the AMTEX. Below $0.5Z_i$, the values of $\gamma_{q\theta}$ are also larger than those of Druilhet *et al.* (over land, poor evaporation, and strong entrainment effects) and those of the BOMEX (Phelps and Pond, 1971).

The correlation $\gamma_{w\theta}$ is ≈ 0.6 below $0.2Z_i$ and decreases to 0.4 near $0.5Z_i$ which is in good agreement with that of Druilhet *et al.*, but larger than that of Phelps and Pond. On the other hand, the correlation γ_{wq} is ≈ 0.55 below $0.5Z_i$ and is ≈ 0.2 larger than those of Phelps and Pond and Druilhet *et al.*, indicating the stronger effect of evaporation for this case.

Figure 8 shows the vertical profiles of the normalized potential temperature and humidity variances. The solid curves

$$\sigma_\theta^2/\theta_*^2 = \sigma_q^2/q_*^2 = 1.8(Z/Z_i)^{-2/3}, \tag{9}$$

are the local free convection form of Wyngaard *et al.* (1971). For the lower half of the MABL, both variances generally follow the $-2/3$ power law of (9), but $\sigma_\theta^2/\theta_*^2$ is smaller than σ_q^2/q_*^2. This is probably related to the fact that positive $\partial\theta/\partial Z$ associated with positive $\overline{w'\theta'}$ destroys σ_θ^2 while negative $\partial q/\partial Z$ associated with positive $\overline{w'q'}$ generates σ_q^2. The larger σ_q^2/q_*^2 at K1 is presumably related to the larger normalized $\overline{w'q'}$, as compared to E1 and E2 (Figure 5b). Near the top of the cloud-free MABL (E1), both normalized variances are much larger than those predicted by local free convection due to entrainment across the MABL

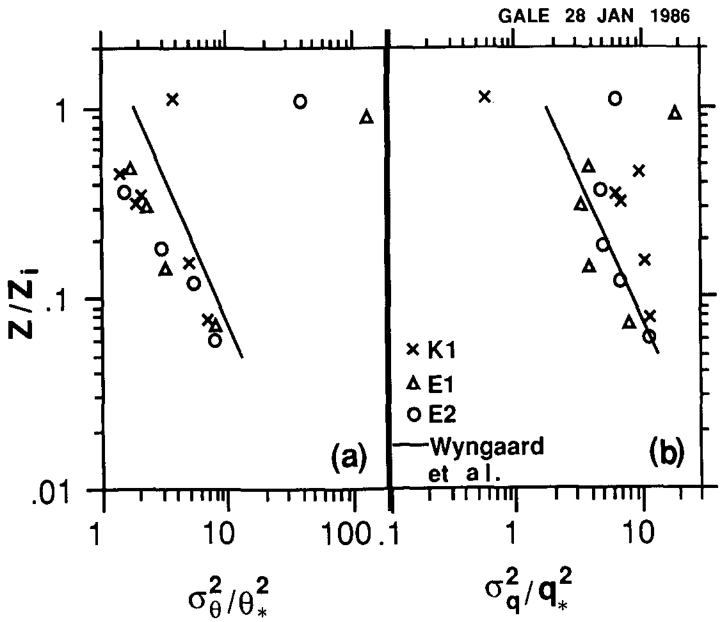

Fig. 8. Vertical profiles of the normalized (a) potential temperature and (b) humidity variances. The solid curves are the local free convection form of Wyngaard *et al.* (1971).

top, where large positive $\partial\theta/\partial Z$ associated with negative $\overline{w'\theta'}$ and large negative $\partial q/\partial Z$ associated with positive $\overline{w'q'}$ could generate large temperature and humidity variances.

Figure 9 shows the vertical profiles of the normalized velocity variances. The maxima are located near $0.3Z_i$ for σ_w^2/w_*^2, but near the surface and Z_i for σ_v^2/w_*^2 (crosswind). The vertical variability for σ_u^2/w_*^2 (alongwind) is very small, being nearly equal to the mid-layer minimum of σ_v^2/w_*^2. The vertical variation in σ_v^2/w_*^2 appears to be highly related to the roll circulations. The solid curve (Figure 9c)

$$\sigma_w^2/w_*^2 = 1.8(Z/Z_i)^{2/3}(1 - 0.8Z/Z_i)^2 \tag{10}$$

indicates the AMTEX results of LWP. The results σ_u^2/w_*^2, σ_v^2/w_*^2 and σ_w^2/w_*^2 are in good agreement with those of the four AMTEX MCC cases of northerly wind (LWP), except for larger σ_v^2/w_*^2 near $0.9Z_i$ due to roll circulation for this case. The data of Chou *et al.* (1986) and this case was observed in the roll vortex regime; however, the normalized velocity variances of this case are much smaller than those of Chou *et al.* (1986). Furthermore, our preliminary analysis indicates that shear production of turbulent kinetic energy is negligibly small in the MABL above the surface layer, which is in better agreement with that of LWP than that of Chou *et al.* These results suggest that MCC and roll vortex regimes can have the same normalized velocity variances (except near the MABL top) if the net energy production by wind shear and buoyancy is about the same. This study

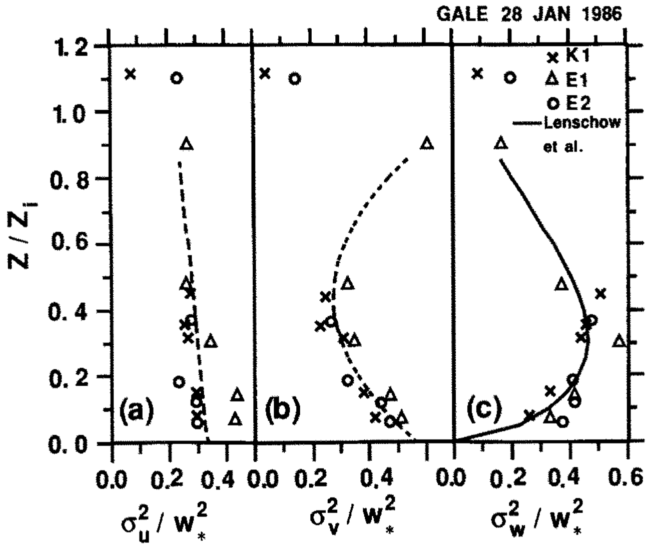

Fig. 9. Vertical profiles of the normalized velocity variances: (a) E–W component (alongwind), (b) N–S component (crosswind), and (c) vertical component. Dashed curves are least-squares fits to the data below $0.5Z_i$. The solid curve is the AMTEX results of Lenschow *et al.* (1980).

further suggests that the difference in normalized velocity variances between Chou *et al.* and LWP is due to the greater shear generation of turbulent kinetic energy near the top and bottom of the MABL in Chou *et al.* and is not due to the difference in convective regimes as was interpreted by those authors.

5. Spectral Distributions

Our next objective is to study the importance of roll circulations in transporting sensible heat and moisture in the MABL. The GOES visible image (Figure 1) indicates that K1, E1, and E2 were in the roll vortex or cloud street regime. Stack E1 was in the cloud-free region, K1 near the cloud edge, and E2 in the uniformly spaced cloud-street region. Thus, the measurements of solar radiation (sr) at E2 are used to determine cloud street (roll) spacing. Figure 10 shows spectra of solar radiation (S_{sr}), normalized by variances, for E2. The solid curve indicates reflected solar radiation near the cloud top, and the other two show the downward solar radiation in the subcloud layer. The parameter n is the frequency, V_a the true air speed, and $f(=nZ_i/V_a)$ the dimensionless frequency. As can be seen from Figure 10, all three normalized spectra have higher spectral densities in the frequency band $f = 0.2$–0.5 and peak at the frequencies near $f = 0.33$. This result indicates that the roll spacing is about three times the MABL depth, in good agreement with previous studies (e.g., LeMone, 1973; Reinking *et al.*, 1981).

The vertical organization of roll circulations in the MABL has also been studied in terms of the spectra of crosswind velocity (S_v), vertical velocity (S_w), potential

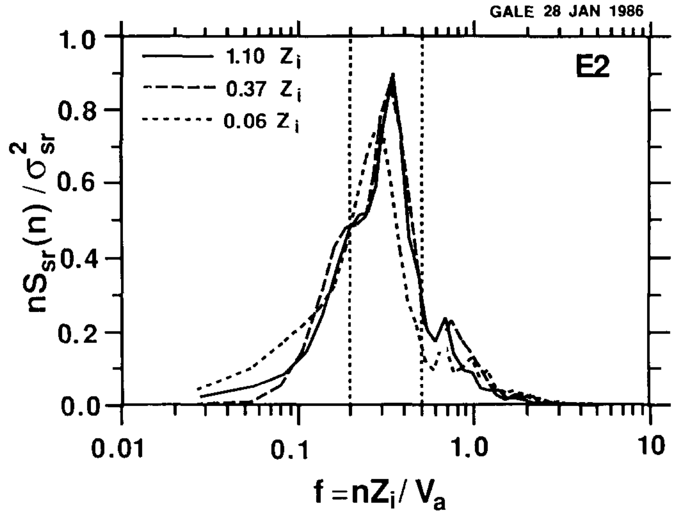

Fig. 10. Spectra of solar radiation (S_{sr}), normalized by variances (σ_{sr}^2), for E2. The solid curve indicates reflected solar radiation near the cloud top, and the dashed curves the downward solar radiation in the subcloud layer. The parameter n is the frequency, V_a the true air speed, and Z_i the inversion base height. The dashed lines at $f = 0.2$ and 0.5 indicate the roll frequency (RF) band.

temperature (S_θ), and humidity (S_q) and cospectra of temperature ($C_{w\theta}$) and humidity fluxes (C_{wq}). Variance normalized S_v, S_w, S_θ, and S_q and covariance normalized $C_{w\theta}$ and C_{wq} for the upper, middle, and lower MABL at E1, E2, and K1 are shown in Figure 11. The spectral results including those beyond $f = 10$ (not shown) indicate that the $-5/3$ law inertial subranges generally exist for S_u (along-wind velocity), S_v, S_w, S_θ, and S_q, except for S_q at K1 and S_θ near Z_i, which falls off more rapidly with frequency than the $-5/3$ spectral slope. The onset of the inertial subrange is near $nZ/V_a = 1$ for surface-layer spectra and near $f = 10$ for those above the surface layer, in good agreement with those of previous studies (e.g., Kaimal *et al.*, 1972, 1976; Chou and Yeh, 1987). In the inertial subranges, cospectral amplitudes of fluxes of momentum, temperature, and humidity decrease rapidly with frequency and are generally negligibly small. It is noted that the results for the inertial subrange are not important for the discussion on roll circulations and fluxes. Therefore, the results beyond $f = 10$ are not shown.

Figure 11 shows that, for the roll scale, the normalized spectra and cospectra all peak at nearly the same normalized frequencies within $f = 0.2$–0.5, near the tops of the surface layer and the MABL, indicating a coherent roll structure. However, the roll vortices appear to be less organized at mid-layer, except for K1. This might be due to the influence of plumes with scale ≈ 600 m. For the roll frequency band $f = 0.2$–0.5, peak frequencies (especially those of the prominent peaks in the upper and lower MABL) are generally located near $f = 0.33$, in good agreement with those derived from solar radiation (Figure 10). Figures 10 and 11 suggest that cloud streets (roll vortices) are vertically organized convection in the

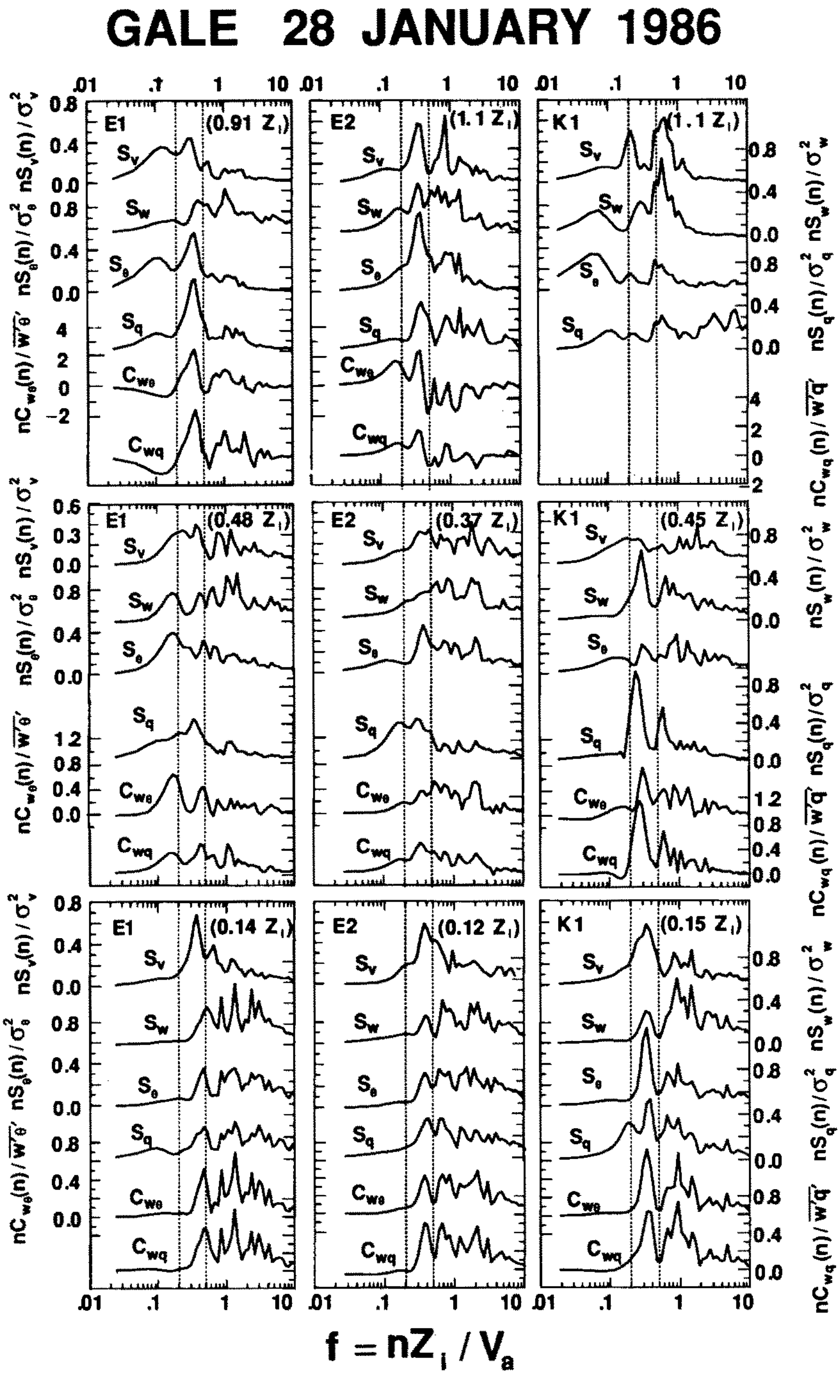

Fig. 11. Spectra of crosswind velocity (S_v), vertical velocity (S_w), potential temperature (S_θ), and humidity (S_q) and cospectra of temperature ($C_{w\theta}$) and humidity fluxes (C_{wq}) for the upper, middle, and lower MABL at E1, E2, and K1. Spectra are normalized by variances, and cospectra by covariances (covariances are positive except $\overline{w'\theta'} < 0$ at $0.9Z_i$ of E1 and $\overline{w'q'} < 0$ at $1.1Z_i$ of E2). Flight levels are indicated in parentheses. Other symbols as in Figure 10.

MABL having the same roll scale for both the cloud layer and subcloud layer, and that the roll spacing is about three times the MABL depth.

The influence of scale on $\overline{w'\theta'}$ and $\overline{w'q'}$ may be studied by dividing the covariance normalized $C_{w\theta}$ and C_{wq} into four spectral regions: $f < 0.2$ ($\lambda > 5$ km), $f =$ 0.2–0.5 ($\lambda = 2$–5 km), $f = 0.5$–5 ($\lambda = 200$m–2 km), and $f = 5$–$10Z_i/V_a$ ($\lambda =$ 10–200 m), where λ is the wavelength. The low-frequency (LF) band $f < 0.2$ contains mesoscale waves or eddies; the roll-frequency (RF) band $f = 0.2$–0.5 contains roll vortices; the medium-frequency (MF) band $f = 0.5$–5 contains the dominant convective thermals in the surface layer and the mixed layer (e.g., Kaimal *et al.*, 1972, 1976; Chou and Yeh, 1987); and the high-frequency (HF) band $f = 5$–$10Z_i/V_a$ contains the small-scale turbulence of the inertial subrange. For the lower half of the MABL, the spectral contributions to the positive $\overline{w'\theta'}$ and $\overline{w'q'}$ primarily come from the RF and MF bands. The contributions from both LF and HF bands are generally very small, except at $0.48Z_i$ of E1 (middle-left panel of Figure 11).

Near the top of the MABL, the turbulent kinetic energy budget is influenced by entrainment, wind shear, radiative cooling, and evaporative cooling (e.g., Lilly, 1968; Zeman and Tennekes, 1977; Randall, 1980; Stage and Businger, 1981; Nicholls, 1989). Therefore, these processes are highly related to the values of $\overline{w'\theta'}$ and $\overline{w'q'}$ near Z_i. Because of the varying strength of roll vortices and thermals, the vertical displacement of the aircraft from the undulating capping inversion is expected to change considerably along the horizontal flight path near Z_i. This further complicates the analysis of data near Z_i (e.g., Jensen and Lenschow, 1978; Mahrt and Paumier, 1982). At $0.9Z_i$ of E1, the aircraft encounters dry air with a 38% mean relative humidity (RH, $\theta_V = 269.6$ K), which fluctuates between the mixed-layer air ($\theta_V = 268.5$ K, RH = 71%) and the inversion top air ($\theta_V = 273$ K, RH = 14%). The negatively buoyant ($-\theta_v'$) air occupies 65% of the time series and the positively buoyant ($+\theta_v'$) air occupies 35% of the time series. At $1.1Z_i$ of E2, the aircraft encounters very dry air with a 11% mean RH ($\theta_V =$ 273.4 K) which fluctuates between the inversion top air ($\theta_V = 275$ K, RH = 5%) and the mixtures ($\theta_V = 270.2$ K, RH = 52%) of cloud air ($\theta_v = 269.8$ K) with entrained air from the inversion. The time series occupied by $+\theta_v'$ and $-\theta_v'$ air are 60 and 40%, respectively. Because of dryness, the difference between θ and θ_V is within 0.1 K for both legs of E1 and E2 near Z_i.

For a thermal-street region, Figure 5 shows that $\overline{w'\theta'}/w_*\theta_*$ equals -0.40 ($\overline{w'\theta_v'}/w_*\theta_{v*} = -0.40$) and $\overline{w'q'}/w_*q_*$ equals 0.10 at $0.9Z_i$ of E1 (clear). This result is mainly due to entrainment of warmer, drier air from the inversion layer and penetration of cooler, wetter air from the MABL. The normalized $C_{w\theta}$ and C_{wq} in the upper-left panel of Figure 11 indicates that entrainment and penetration prevail in the RF and MF bands. The remarkable peaks near $f = 0.33$ suggest a strong penetrative effect of cooler, wetter air near the updraft branches of roll vortices and a strong entrainment effect of warmer drier air near the downdraft branches. The normalized $C_{w\theta}$ and C_{wq} are negative for the LF band, suggesting that the LF wave and/or turbulence activity tend to counteract the effect of entrainment and penetration near Z_i.

For a cloud-street region, these two fluxes near Z_i atop a cloudy MABL are quite different from those of a clear MABL. Figure 5 shows that $\overline{w'\theta'}/w_*\theta_*$ equals 0.20 ($\overline{w'\theta_v'}/w_*\theta_{v*} = 0.19$) and $\overline{w'q'}/w_*q_*$ equals -0.15 at $1.1Z_i$ of E2 (cloudy). This result is primarily because evaporative cooling, which tends to have a positive contribution to $\overline{w'\theta'}$ and negative contribution to $\overline{w'q'}$, strongly affects the fluxes near the cloud top. The analysis based on the bivariate conditional sampling technique (e.g., CZ) reveals that negatively buoyant downdrafts (16% of the time series) are cooler and wetter than negatively buoyant penetrative updrafts (24% of the time series), indicating an evaporative cooling effect of cloud droplets on the mixtures of cloudy air and the entrained air from the capping inversion. The normalized $C_{w\theta}$ and C_{wq} in the center-top panel of Figure 11 show that evaporative cooling prevails in the LF and RF bands; while entrainment and penetration dominate in the MF band. The data (sr, q_l', q', θ_v', w', $w'\theta_v'$, and $w'q'$) shown in Figure 12 indicate that the evaporatively cooled and moistened air parcels, which are unsaturated mixtures (RH $\leq$ 52%) located below (or above) the diffused cloud top and near the edges of the roll-scale dry downdrafts, are primarily responsible for the dominant peak near $f = 0.33$ for the normalized $C_{w\theta}$ and C_{wq} at $1.1Z_i$ of E2.

Near the MABL top, $\overline{w'q'}$ is opposite to $\overline{w'\theta'}$ (Figure 5); therefore $C_{w\theta}$ and C_{wq} are negatively correlated, especially for the roll-scale. This result is related to the upward sharp increase in θ and rapid decrease in q near Z_i (Figure 4). The cospectra $C_{q\theta}$ normalized by $\overline{q'\theta'}$ (humidity-temperature covariance) for $0.9Z_i$ of E1 and $1.1Z_i$ of E2 are shown in Figure 13. Near Z_i, $\gamma_{q\theta}$ and $\overline{q'\theta'}$ are negative (see Figures 7 and 12). Hence, Figure 13 suggests negative correlation between q and θ for all scales near Z_i, especially for the roll-scale.

Figures 10, 11, and 13 all indicate that roll circulations are highly organized with strong signals near the MABL top. The circulations near Z_i may be visualized as follows. Near Z_i of the clear thermal-street region (E1), the updraft branches of roll circulations transport wetter and cooler air upward, while the downdraft branches transport the entrained drier and warmer air downward. Thus, roll circulations, which carry q–θ highly negatively correlated air parcels (Figure 13), transfer sensible heat downward ($C_{w\theta} < 0$) and moisture upward ($C_{wq} > 0$). Because the air is very dry, the difference between buoyancy flux ($\overline{w'\theta_v'}$) and temperature flux ($\overline{w'\theta'}$) is within 2% of ($\overline{w'\theta'}$) for the leg of E1 (and E2) near Z_i. Thus, the roll vortices in the clear thermal-street regions consume turbulent kinetic energy, but increase potential energy through entrainment and penetration.

On the other hand, near Z_i of the cloud-street region (E2), the updraft branches of roll circulations transport wetter and cooler air upward, while the downdraft branches not only transport the entrained drier and warmer air downward in the dry regions, but also transport the wettest and coolest air (probably caused by the evaporative cooling of cloud droplets diffused from the overturning cloud air near

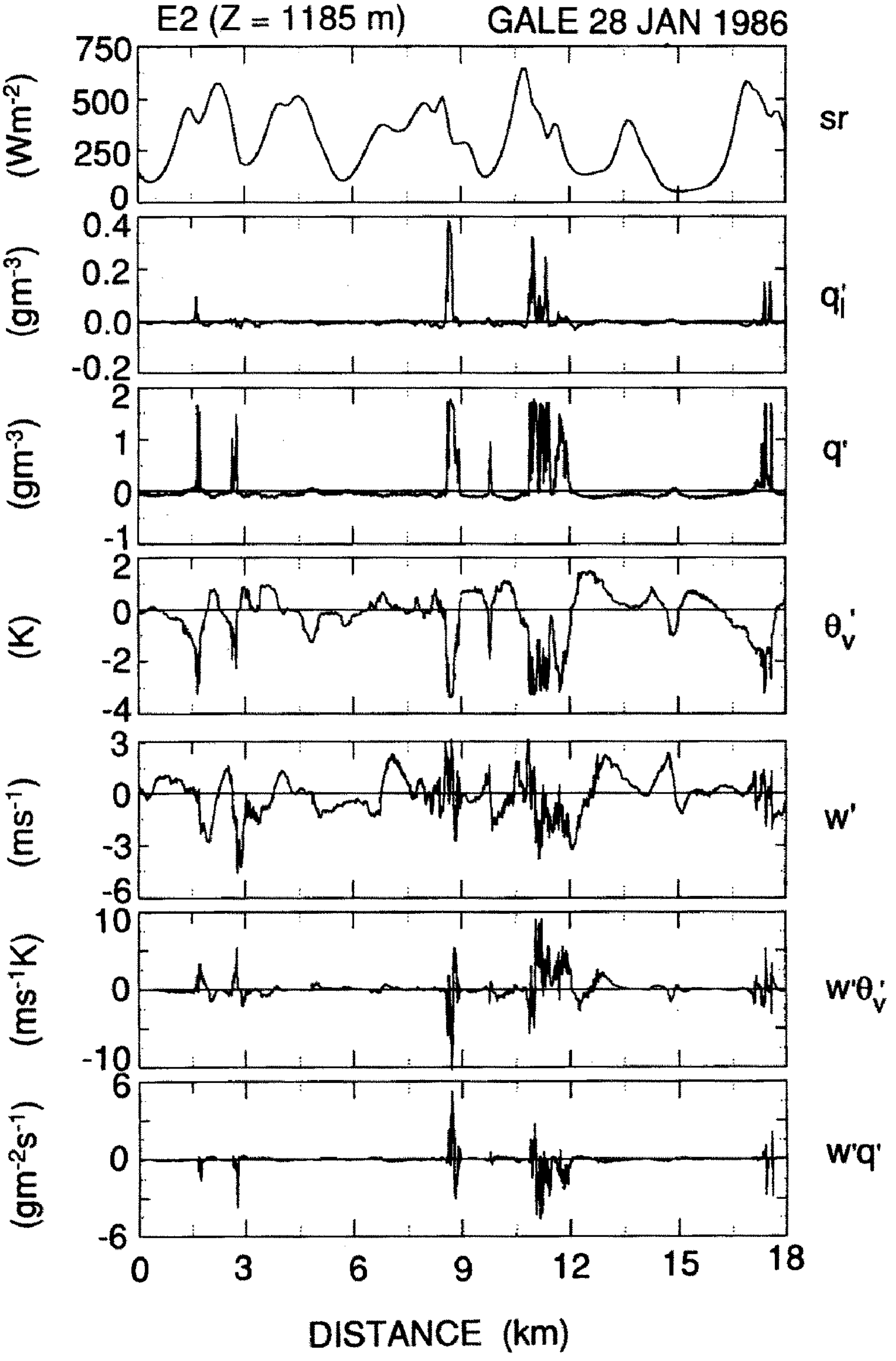

Fig. 12. Fluctuations of 1-Hz reflected solar radiation (sr), detrended 20-Hz liquid water content (q_l'), absolute humidity (q'), virtual potential temperature (θ_v') and vertical velocity (w'), and turbulent fluxes ($w'\theta_v'$ and $w'q'$) from the NCAR Electra on a horizontal crosswind run near the cloud top at E2. True air speed is $\approx 100\,\mathrm{m\,s^{-1}}$. Data ($q_l'$, q', θ_v', and w') are linearly detrended from 5-minute segment.

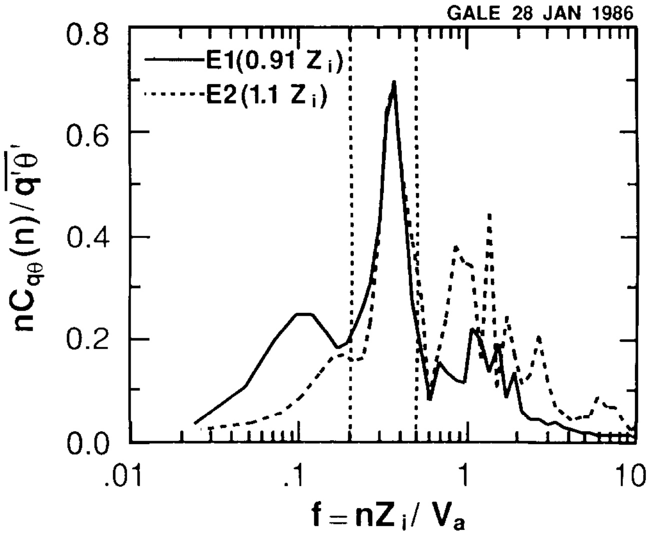

Fig. 13. Temperature-humidity cospectra ($C_{q\theta}$), normalized by covariance ($\overline{q'\theta'}$) for $0.9Z_i$ of E1 (solid curve) and $1.1Z_i$ of E2 (dashed curve). Other symbols as in Figure 10.

Z_i) downward in the regions between the roll-scale wet updrafts and dry downdrafts (Figure 12). Therefore, the evaporative-cooling influenced roll circulations, which also carry q–θ highly negatively correlated air parcels (Figures 12 and 13), transfer sensible heat upward ($C_{w\theta} > 0$) and moisture downward ($C_{wq} < 0$). It is generally known that cloud-top entrainment instability is characterized by an upward buoyancy flux at the cloud top, which can generate turbulent kinetic energy and enhance entrainment near the cloud top (e.g., Randall; Deardorff, 1980; Mahrt and Paumier, 1982). However, at E2, $\Delta\theta_e$ (the jump of equivalent potential temperature across Z_i from above to below) is positive and $\overline{w'\theta_v'} > 0$ is not consistent with the jump criterion of instability. Instead, the dominant scales are consistent among clouds (Figure 10), roll vortices (Figure 11), and the upward buoyancy flux due to evaporative cooling ($C_{w\theta}$ in the center top panel of Figure 11). This result suggests that the effect of the evaporative cooling on generating buoyancy flux is highly related to the circulation patterns of the roll vortices near Z_i. The negatively buoyant downdrafts may result from the horizontal convergence of the upper branches of roll circulations constrained by the inversion. Near Z_i, the updraft branches of roll circulations may spread out under the inversion and pass over the cloud-top interface. Therefore, the negatively buoyant cloud air in the upper updraft branches (which may also incorporate the radiatively cooled air) may mix with the inversion air to generate the coolest air by evaporative cooling. The coolest air may then be forced down in the downdraft branches of roll circulations.

According to Nicholls (1989), cloud-top radiative cooling is an important mechanism for generating negatively buoyant downdrafts and positive ($\overline{w'\theta_v'}$) near the top of stratocumuli. It is likely that the radiative cooling near the cloud tops

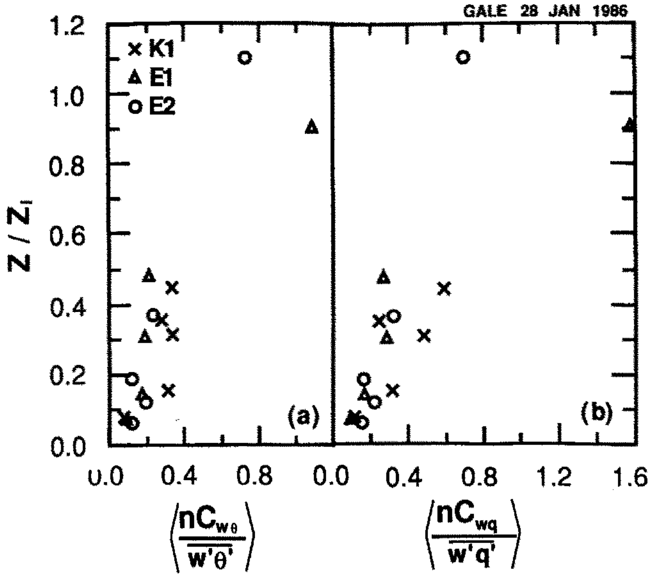

Fig. 14. Vertical profiles of fractional contributions to (a) temperature and (b) humidity fluxes from the roll frequency (RF) band $f = 0.2$–0.5.

(updraft regions of roll circulations) already enhances the measured $(\overline{w'\theta_v'})$ and $C_{w\theta}$ in the RF band near Z_i of E2. However, it is not clear that the cloud-top radiative cooling plays a very important role in the cloud-street region, as compared to evaporative cooling.

Figure 14 shows the vertical profiles of fractional contributions $\langle nC_{w\theta}/\overline{w'\theta'}\rangle$ and $\langle nC_{wq}/\overline{w'q'}\rangle$ from the RF band. Here the fractional contribution $\langle nC_{wx}/\overline{w'x'}\rangle$ is defined as

$$\langle nC_{wx}/\overline{w'x'}\rangle = \int_{0.2}^{0.5} nC_{wx}(n)\, df/\overline{w'x'}\,, \tag{11}$$

and $x = \theta$ or q. It can be seen that both contributions increase with height, especially near Z_i. At $0.9Z_i$ of E1, the fractional fluxes contributed by the RF band are greater than the total fluxes integrated over the whole spectrum (flight-level fluxes); these fractional fluxes are about 1.1 of $(\overline{w'\theta'})$ and 1.60 of $(\overline{w'q'})$. At $1.1Z_i$ of E2, the RF band contributes about 0.7 of the flux to both $(\overline{w'\theta'})$ and $(\overline{w'q'})$. Figure 14 suggests that the importance of roll vortices in transporting sensible heat and moisture increases upward, and that the transport of sensible heat and moisture near Z_i is primarily carried out by roll circulations in the roll vortex regime. This finding is consistent with previous studies (e.g., LeMone, 1973; CZ).

6. Conclusions

Turbulence and heat fluxes in the MABL for three aircraft stacks (K1, E1, and E2) near the western Gulf Stream front, observed during the GALE 28 January 1986 cold-air outbreak, have been studied using mixed-layer scaling (Figure 1). The GOES image and stability parameter $-Z_i/L$ indicate that these three stacks were in the roll vortex regime (LeMone, 1973). Stack E1 was in the thermal-street region (cloud free), K1 near the cloud edge, and E2 in the cloud-street region. The crosswind stacks at E1 and E2 were nearly parallel to the SST isotherms, while that at K1 was nearly perpendicular to the SST isotherms with stronger SST gradient. Across the Gulf Stream front, the total surface flux of sensible and latent heat increased from 550 $\mathrm{W\,m^{-2}}$ (E1, SST = 14 °C) to 1000 $\mathrm{W\,m^{-2}}$ (E2, SST = 20 °C).

The normalized spectra and cospectra (solar radiation, velocity, potential temperature, humidity, and heat fluxes) peak near $f = 0.33$ ($f = nZ_i/V_a$ = MABL depth/wavelength, Figures 10 and 11). This result suggests that cloud streets (roll vortices) are vertically organized convection in the MABL having the same roll scale for both the cloud layer and subcloud layer, and that the roll spacing is about three times the MABL depth. The roll circulations contribute significantly to the sensible heat and moisture fluxes. For the lower half of the MABL, the contributions to the positive $\overline{w'\theta'}$ and $\overline{w'q'}$ mainly come from the roll-frequency (RF, $f = 0.2$–0.5) and medium-frequency (MF, $f = 0.5$–5) bands (Figure 11). The RF band contains roll vortices; the MF contains the dominant convective thermals in both the unstable surface and mixed layers (e.g., Kaimal *et al.*, 1972, 1976; Chou and Yeh, 1987). The results also suggest that the importance of roll vortices in transporting sensible heat and moisture increases upward, and that these transports near Z_i are primarily carried out by roll circulations in the roll vortex regime (Figures 11 and 14). These results are in good agreement with previous studies (e.g., LeMone, 1973, 1976, Reinking *et al.*, 1981; CZ).

Near the MABL top, roll circulations are highly organized with strong signals (Figures 10, 11, and 13). For the clear thermal-street region (El), the updraft branches of roll circulations transport wetter and cooler air upward, while the downdraft branches transport the entrained drier and warmer air downward. Thus, roll circulations, which carry q–θ highly negatively correlated air parcels, transfer sensible heat downward ($C_{w\theta} < 0$) and moisture upward ($C_{wq} > 0$). This negative $C_{w\theta}$ suggests that roll vortices consume turbulent kinetic energy while increasing potential energy through entrainment and penetration near Z_i of the clear thermal-street region.

On the other hand, near Z_i of the cloud-street region (E2), the updraft branches of roll circulations transport wetter and cooler air upward, while the downdraft branches not only transport the entrained drier and warmer air downward in the dry region, but also transport the wettest and coolest air (probably caused by the evaporative cooling of cloud droplets diffused from the overturning cloud air near Z_i) downward in the regions between the roll-scale wet updrafts and dry downdrafts (Figure 12). Therefore, the evaporative-cooling influenced roll circulations, which also carry q–θ highly negatively correlated air parcels (Figures 12 and 13), transfer sensible heat upward ($C_{w\theta} > 0$) and moisture downward ($C_{wq} < 0$). The dominant scales are consistent among clouds (Figure 10), roll vortices, and the upward buoyancy flux due to evaporative cooling (Figure 11), suggesting that the effect of evaporative cooling on generating buoyancy flux is highly related to the circulation patterns of roll vortices near the inversion.

For the lower half of the MABL, the normalized temperature flux decreases upward more rapidly than the humidity flux (Figure 5). This behavior is likely to be related to the entrainment effects at Z_i, which tend to influence the lapse rates of θ and q in the mixed layer but not in the unstable surface layer. The normalized budgets of both fluxes are compared to gain some insight about this phenomenon (Figure 6). Gradient production (GP) appears to be the major cause for the discrepancy. Gradient production (GP) is a sink for $\overline{w'\theta'}$ because of positive $\partial\bar{\theta}/\partial Z$, but is a source for $\overline{w'q'}$ due to negative $\partial\bar{q}/\partial Z$. For the lower mixed layer, buoyant production (BP) and gradient production (GP) are sources for $\overline{w'q'}$ to balance the sink due to pressure transport (Pr), while BP and Pr are sources for $\overline{w'\theta'}$ to balance the sink due to GP. On the other hand, both budgets of $\overline{w'\theta'}$ and $\overline{w'q'}$ are generally expected to be fairly similar in the unstable surface layer, where GP and BP act as sources for both $\overline{w'\theta'}$ and $\overline{w'q'}$ to balance the sinks due to Pr (e.g., Wyngaard *et al.*, 1971; LWP). Figure 6 suggests that $\overline{w'\theta'}$ decreases upward more sharply than $\overline{w'q'}$ mainly because GP is a source for $\overline{w'\theta'}$ in the unstable surface layer, but changes to a sink in the mixed layer, while GP acts as a source for $\overline{w'q'}$ in both the unstable surface and mixed layers.

Acknowledgements

We should like to acknowledge R. L. Grossman, A. J. Riordan, T. Holt, T. J. Mercer, C. Velden, and the flight crews and observers of the NCAR Electra and King Air aircraft for obtaining and providing the excellent data. We are grateful to R. L. Grossman for providing the Lyman-Alpha calibration routine and many valuable discussions. Helpful comments on the manuscript from M. A. LeMone, L. Mahrt, and an anonymous reviewer are highly appreciated. We also thank Patty Golden for expertly typing the manuscript, and J. Zimmerman for assistance with data analysis.

Appendix

TURBULENT TRANSPORT CALCULATIONS

Turbulent profiles of the normalized third moments are shown in Figure A1. Following the approach of LWP, in which both third moments were assumed to decrease linearly with height in the bulk of the MABL, the normalized third moments may be parameterized as

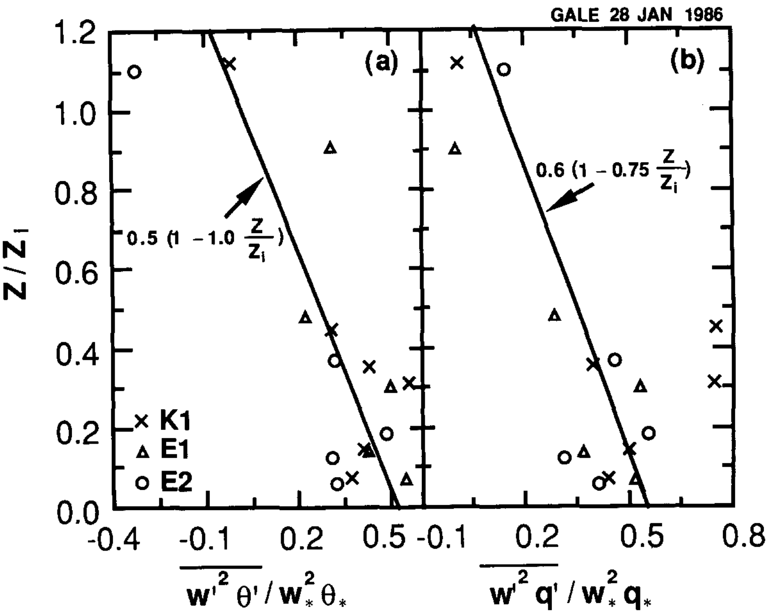

Fig. A1. Vertical profiles of the normalized third moments: (a) $\overline{w'^2\theta'}/w_*^2\theta_*$ and (b) $\overline{w'^2q'}/w_*^2q_*$. Solid curves are least-squares fits.

$$\overline{w'^2\theta'}/w_*^2\theta_* = 0.5(1 - 1.0Z/Z_i)\,, \tag{A1}$$

$$\overline{w'^2q'}/w_*^2q_* = 0.6(1 - 0.75Z/Z_i)\,. \tag{A2}$$

Parameterization (A1) fits $\overline{w'^2\theta'}$ data well except for E1 and E2 near Z_i; (A2) is also a good fit for $\overline{w'^2q'}$ except for E1 near Z_i and K1 near $0.4Z_i$. Figure 11 suggests that the RF band contributes significantly to large scatter from (A1) and (A2) near Z_i for E1 and E2 and near $0.4Z_i$ for K1. Both (A1) and (A2) are used to derive the turbulent transport (Tr) for the normalized budgets of $\overline{w'\theta'}$ and $\overline{w'q'}$ in Figure 6. According to (A1) and (A2), turbulent transport (Tr) for $\overline{w'\theta'}$ and $\overline{w'q'}$ are 0.5 and 0.45, respectively. Therefore, the contributions of Tr to both budgets are about the same and much smaller than those of the other budget terms. This result is in good agreement with that of LWP.

References

Agee, E. M. and Howley, R. P.: 1977, 'Latent and Sensible Heat Flux Calculations at the Air-Sea Interface During AMTEX 74', *J. Appl. Meteorol.*, **16**, 443–447.

Bane, J. M. and Osgood, K. E.: 1989, 'Wintertime Air-Sea Interaction Processes Across the Gulf Stream', *J. Geophys. Res.* **94**, 10,755–10,722.

Budyko, M. I.: 1963, 'Atlas of Heat Balance of the Earth's Surface', USSR Glavnaia Geofizicheskaia Observatoriia, Moscow, 69 pp.

Bunker, A. and Worthington, L. V.: 1976, 'Energy Exchange Charts of the North Atlantic Ocean', *Bull. Amer. Meteorol Soc.* **57**, 450–467.

Chou, S.-H. and Yeh, E.-N.: 1987, 'Airborne Measurements of Surface Layer Turbulence over the Ocean During Cold Air Outbreaks', *J. Atmos. Sci.* **44**, 3721–3733.

Chou, S.-H. and Zimmerman, J.: 1989, 'Bivariate Conditional Sampling of Buoyancy Flux during an Intense Cold-Air Outbreak', *Boundary-Layer Meteorol.* **46**, 93–112.

Chou, S.-H., Atlas, D. and Yeh, E.-N.: 1986, 'Turbulence in a Convective Marine Atmospheric Boundary Layer', *J. Atmos. Sci.* **43**, 547–564.

Deardorff, J. W.: 1972, 'Numerical Investigation of Neutral and Unstable Planetary Boundary Layers', *J. Atmos. Sci.* **29**, 91–115.

Deardorff, J. W.: 1980, 'Cloud Top Entrainment Instability', *J. Atmos. Sci.* **37**, 131–147.

Deardorff, J. W.: 1985, 'Laboratory Experiments on Diffusion: The Use of Convective Mixed-Layer Scaling', *J. Clim. Appl. Meteorol.* **24**, 1143–1151.

Dirks, R. A., Kuettner, J. P., and Moore, J. A.: 1988, 'Genesis of Atlantic Lows Experiment (GALE): An Overview', *Bull. Amer. Meteorol. Soc.* **69**, 148–160.

Druilhet, A., Frangi, J. P., Guedalia, D. and Fontan, J.: 1983, 'Experimental Studies of the Turbulence Structure Parameters of the Convective Boundary Layer', *J. Clim. Appl. Meteorol.* **22**, 594–608.

Friehe, C. A., Grossman, R. L., and Pann, Y.: 1986, 'Calibration of an Airborne Lyman-Alpha Hygrometer and Measurement of Water Vapor Flux Using a Thermoelectric Hygrometer', *J. Atmos. and Ocean. Tech.* **3**, 299–304.

Grossman, R. L.: 1982, 'An Analysis of Vertical Velocity Spectra Obtained in the BOMEX Fair-Weather, Trade-Wind Boundary-Layer', *Boundary-Layer Meteorol.* **23**, 323–357.

Grossman, R. L. and Betts, A. K.: 1990, 'Air-Sea Interaction During an Extreme Cold Air Outbreak from the Eastern Coast of the United States', *Mon. Wea. Rev.* **118** (in press).

Jenkins, G. M. and Watts, D. G.: 1968, *Spectral Analysis and its Application*, Holden-Day, 525 pp.

Jensen, N. O. and Lenschow, D. H.: 1978: 'An Observational Investigation of Penetrative Convection', *J. Atmos. Sci.* **35**, 1924–1933.

Kaimal, J. C., Wyngaard, J. C., Izumi, Y., and Cote, O. R.: 1972, 'Spectral Characteristics of Surface-Layer Turbulence', *Quart. J. Roy. Meteorol. Soc.* **98**, 563–589.

Kaimal, J. C., Wyngaard, J. C., Haugen, D. A., Coté, O. R., Izumi, Y., Caughey, S. J., and Readings, C. J.: 1976, 'Turbulence Structure in the Convective Boundary Layer', *J. Atmos. Sci.* **33**, 2152–2169.

Kondo, J.: 1975, 'Air-Sea Bulk Transfer Coefficients in Diabatic Conditions', *Boundary-Layer Meteorol.* **9**, 91–112.

Kung, E. C. and Siegel, A. J.: 1979, 'A Study of Heat and Moisture Budgets in the Intense Winter Monsoon over the Warm Ocean Current', *J. Atmos. Sci.* **36**, 1880–1894.

Lanczos, C.: 1956, *Applied Analysis*, Prentice Hall, Englewood Cliffs, NJ, 539 pp.

LeMone, M. A.: 1973, 'The Structure and Dynamics of Horizontal Roll Vortices in the Planetary Boundary Layer', *J. Atmos. Sci.* **30**, 1077–1091.

LeMone, M. A.: 1976, 'Modulation of Turbulence Energy by Longitudinal Rolls in an Unstable Boundary Layer', *J. Atmos. Sci.* **33**, 1308–1320.

LeMone, M. A. and Pennell, W. T.: 1980, 'A Comparison of Turbulence Measurements from Aircraft', *J. Appl. Meteorol.* **19**, 1420–1437.

Lenschow, D. H., Wyngaard, J. C., and Pennell, W. T.: 1980, 'Mean-Field and Second-Moment Budgets in a Baroclinic, Convective Boundary Layer', *J. Atmos. Sci.* **37**, 1313–1326.

Lilly, D. K.: 1968, 'Models of Cloud-Topped Mixed Layers under a Strong Inversion', *Quart. J. Roy. Meteorol. Soc.* **94**, 292–309.

Mahrt, L.: 1976, 'Mixed Layer Moisture Structure', *Mon. Wea. Rev.* **104**, 1403–1407.

Mahrt, L. and Paumier, J.: 1982, 'Cloud-Top Entrainment Instability Observed in AMTEX', *J. Atmos. Sci.* **39**, 622–634.

Nicholls, S.: 1984, 'The Dynamics of Stratocumulus: Aircraft Observations and Comparisons with a Mixed Layer Model', *Q.J.R. Meteorol. Soc.* **110**, 783–820.

Nicholls, S.: 1989, 'The Structure of Radiatively Driven Convection in Stratocumulus', *Q.J.R. Meteorol. Soc.* **115**, 487–511.

Nicholls, S. and LeMone, M. A.: 1980, 'The Fair Weather Boundary Layer in GATE: The Relationship of Subcloud Fluxes and Structure to the Distribution and Enhancement of Cumulus Clouds', *J. Atmos. Sci.* **37**, 2051–2067.

Pennell, W. T. and LeMone, M. A.: 1974, 'An Experimental Study of Turbulence Structure in the Fair-Weather Trade Wind Boundary Layer', *J. Atmos. Sci.* **31**, 1308–1323.

Phelps, G. T. and Pond, S.: 1971, 'Spectra of the Temperature and Humidity Fluctuations and of the Fluxes of Moisture and Sensible Heat in the Marine Boundary Layer', *J. Atmos. Sci.* **28**, 918–928.

Randall, D. A.: 1980, 'Conditional Instability of the First Kind Upside Down', *J. Atmos. Sci.* **37**, 125–130.

Reinking, R. F., Doviak, R. J., and Gilmer, R. O.: 1981, 'Clear-Air Roll Vortices and Turbulent Motions as Detected with an Airborne Gust Probe and Dual-Doppler Radar', *J. Appl. Meteorol.* **20**, 678–685.

Reitan, C. H.: 1974, 'Frequencies of Cyclones and Cyclogenesis for North America, 1951–1970', *Mon. Wea. Rev.* **102**, 861–868.

Sanders, F. and Gyakum, J. R.: 1980, 'Synoptic Dynamic Climatology of the Bomb', *Mon. Wea. Rev.* **108**, 1589–1606.

Sheu, P. J. and Agee, E. M.: 1977, 'Kinematic Analysis and Air-Sea Heat Flux Associated with Mesoscale Cellular Convection During AMTEX 75', *J. Atmos. Sci.* **34**, 793–801.

Stage, S. A. and Businger, J. A.: 1981, 'A Model for Entrainment into a Cloud-Topped Marine Boundary Layer. Part II: Discussion of Model Behavior and Comparison with Other Models', *J. Atmos. Sci.* **38**, 2230–2242.

Warsh, K. L.: 1973, 'Relation of Air-Sea Interface Energy Fluxes to Convective Activity in the Tropical Atlantic Ocean', *J. Geophys. Res.* **78**, 504–510.

Willis, G. E. and Deardorff, J. W.: 1974, 'A Laboratory Model of the Unstable Planetary Boundary Layer', *J. Atmos. Sci.* **31**, 1297–1307.

Wyngaard, J. C., Coté, O. R., and Izumi, Y.: 1971, 'Local Free Convection, Similarity, and the Budgets of Shear Stress and Heat Flux', *J. Atmos. Sci.* **28**, 1171–1182.

Wyngaard, J. C., Pennell, W. T., Lenschow, D. H., and LeMone, M. A.: 1978, 'The Temperature-Humidity Covariance Budget in the Convective Boundary Layer', *J. Atmos. Sci.* **35**, 47–58.

Zeman, O. and Tennekes, H.: 1977, 'Parameterization of the Turbulent Energy Budget at the Top of the Daytime Atmospheric Boundary Layer', *J. Atmos. Sci.* **34**, 111–123.